Resonance-Based Directional Light Emission from Organic Light-Emitting Diodes: Comparing Integrated Nanopatterns and Color Conversion Waveguide Gratings

Janek Buhl,* Hannes Lüder, Gitta Bichmann, Tim Nolte, Adrian Petraru, and Martina Gerken*

Tailoring the angular emission pattern of organic light-emitting diodes (OLEDs) is a promising approach to increase device performance in many applications. In miniaturized point-of-need sensor systems using organic light sources and photodetectors, directional illumination of specific sensing spots may enhance overall sensitivity by improved light utilization. Periodically nanopatterned waveguides forming photonic crystal slabs are oftentimes employed to obtain directional resonant light outcoupling from OLEDs. This work compares emission directionality for two types of devices utilizing the same polymer compounds as the emissive material: OLEDs comprising a nanopatterned bottom electrode and conventional OLEDs featuring a dedicated nanopatterned color conversion layer (CCL) for directional light outcoupling. Simulated and experimentally measured emission characteristics show that resonant outcoupling effects from a separate CCL are significantly stronger due to spatial separation from the lossy electrode layers as well as high optical contrast at the waveguide interfaces. While OLEDs with nanopatterned electrodes exhibit only small deviations from the Lambertian emission profile, the nanopatterned CCL induces high outcoupling peaks at specific viewing angles leading to increased emission directionality.

1. Introduction

Organic light-emitting diodes (OLEDs) are thin-film devices employing organic semiconducting materials for light generation. In contrast to conventional inorganic LEDs, OLEDs are inherently surface emitters offering favorable properties such as the possibility to fabricate fully transparent or flexible devices.[1] In display applications, OLED panels are widely used due to their high color contrast and wide viewing angles.[2] Moreover, OLEDs also hold great potential for numerous different applications including general lighting, optical signage, and sensing.[3–6] The organic multilayer stack of the OLED facilitates modifications of device properties to match individual application requirements. Additionally, solution-based manufacturing methods for organic optoelectronics allow for cost-efficient device fabrication, making OLEDs favorable candidates for point-of-need applications or recyclable single-use devices.

OLED illuminants typically feature homogeneous wide-angle light emission suitable for large-area and indirect lighting. However, in other scenarios, narrow-angle light emission and directional illumination of specific areas are desired. We have previously demonstrated a miniaturized optical sensing unit for point-of-need analysis comprising several pairs of OLED light sources and organic photodetectors on a single substrate.[7] Directional light emission toward the sensing spots may significantly increase the light utilization ratio and overall system sensitivity in the proposed side-by-side configuration.[8] In conventional sensing systems, additional components are typically used to adjust the optical path and focus light onto the sensing area. In the case of highly miniaturized sensors which do not allow for any assembly or alignment steps, all optical elements must be integrated directly into the devices.

Most of the studies on directional OLED emission focus on thermally evaporated small molecules. While these materials usually provide high device performance with respect to luminance and efficiency, they also require vacuum processing, leading to increased manufacturing costs. Solution-based large-scale fabrication methods, such as slot-die coating or inkjet printing, in contrast, may provide reasonably affordable organic optoelectronics for disposable sensing units. Solution-processed device stacks generally comprise polymer semiconductors whose optical properties must be taken into consideration.

A well-known approach to obtain angle-dependant light emission is resonant outcoupling of quasi-guided optical modes from

J. Buhl, H. Lüder, G. Bichmann, T. Nolte, A. Petraru, M. Gerken
Faculty of Engineering
Kiel University
Kaiserstr. 2, 24143 Kiel, Germany
E-mail: jabu@tf.uni-kiel.de; mge@tf.uni-kiel.de

J. Buhl, H. Lüder, G. Bichmann, T. Nolte, A. Petraru, M. Gerken
Kiel Nano, Surface and Interface Science KiNSIS
Kiel University
Christian-Albrechts-Platz 4, 24118 Kiel, Germany

ADVANCED
SCIENCE NEWS

www.advancedsciencenews.com

ADVANCED
PHOTONICS
RESEARCH
Open Access

www.adpr-journal.com

a periodically nanopatterned waveguide forming a photonic crystal slab.[9,10] Light propagates inside a slab waveguide in the form of guided modes. A guided mode is an electromagnetic wave, mostly confined in the high-index layer, which propagates along the waveguide without changing its field profile. Depending on the polarization of the electric and the magnetic field with respect to the propagation direction, guided modes are divided into transverse electric (TE) and transverse magnetic (TM) modes. A mode propagating along the x-axis (see **Figure 1** for an illustration of the grating waveguide structure and the corresponding coordinate system) is characterized by its wave vector $k = k_{\text{mode}}e_x$ or, equivalently, by its effective refractive index

$$n_{\text{eff}} = \frac{k_{\text{mode}}}{k_0} \tag{1}$$

where $k_0 = 2\pi/\lambda_0$ is the free-space wave number. For all guided modes, n_{eff} is larger than the refractive indices of the surrounding media. For any wave in free space, the in-plane component of its wave vector is given as

$$k_x = k_0 \sin(\vartheta) < k_0 < k_{\text{mode}} \tag{2}$$

where ϑ is the angle of the propagation direction with respect to the slab waveguide's surface normal. Therefore, guided modes cannot couple to incident or outgoing plane waves because the necessary momentum conservation cannot be fulfilled. The introduction of a periodic refractive index modulation along the x-axis, creating a photonic crystal slab, leads to Bragg scattering of the guided modes. As long as the refractive index modulation is sufficiently weak, the in-plane wavenumber after scattering can be written as

$$k'_{\text{mode}} = k_{\text{mode}} + m \cdot G, \qquad m \in \mathbb{Z} \tag{3}$$

where $G = 2\pi/\Lambda$ is the reciprocal grating vector. If k'_{mode} falls into the light cone $|k'_{\text{mode}}| < k_0$ for any $m \in \mathbb{Z}$, the scattered mode will couple to the far field with an out-coupling angle $\sin(\vartheta) = k'_{\text{mode}}/k_0$. Typically, $m = -1$, yielding[11]

$$\sin(\vartheta) = n_{\text{eff}} - \frac{\lambda_0}{\Lambda} \tag{4}$$

Consequently, the grating in the waveguide turns a guided into a quasi-guided mode that leaks energy into the far field. For each optical mode, condition (4) is truly satisfied for one specific wavelength at a fixed viewing angle ϑ, resulting in resonant out-coupling peaks that follow the mode's dispersion relation.

Integrated photonic crystal structures in OLEDs may lead to enhanced outcoupling of waveguided modes, improving device efficiency and modifying angular emission characteristics.[12–14] They are commonly fabricated by either depositing the bottom electrode onto a nanopatterned layer or patterning the electrode itself.[15] The photonic crystal slab is consequently formed by the entire layer stack. Significant changes to the emission characteristics of OLEDs have been achieved with this approach.[16–18] However, light directionality is usually limited due to the high absorption of the electrode layers reducing the propagation length in the waveguide. Additionally, many of the organic polymer semiconductors used in solution-processed OLED stacks exhibit high refractive indices close to that of indium tin oxide (ITO), which is the most commonly used electrode material. Since the resulting optical contrast is comparatively low, it is even more difficult to achieve directional emission from devices comprising high-index polymer materials.

Highly directional outcoupling of substrate modes can also be obtained by placing a diffractive optical element adjacent to the OLED while blocking nondirectional direct emission.[19] Although this approach allows confinement of the emissive light to a very narrow cone angle, only a small fraction of the total OLED light is utilized, making it unfavorable for point-of-need sensing applications. As an alternative approach, we propose the application of a nanopatterned fluorescent waveguide in
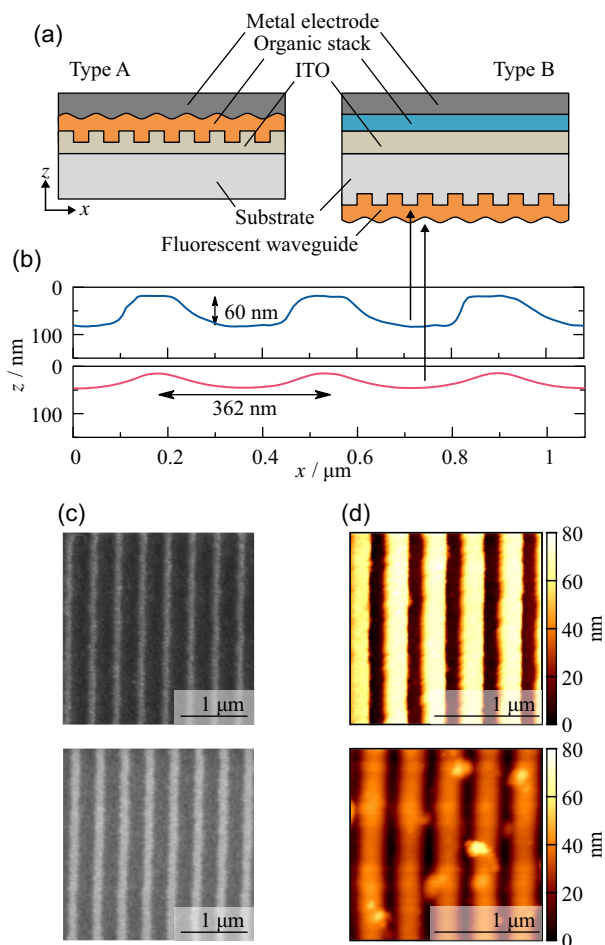

Figure 1. a) Schematic representation of the device structures. Device type A: organic light-emitting diode (OLED) with a nanopatterned indium tin oxide (ITO) bottom-electrode. Device type B: OLED with a nanopatterned fluorescent waveguide layer. b) The deposited polymer layer leads to attenuation of the integrated nanopattern, as apparent in the surface profiles of the type B device measured by atomic force microscopy (AFM). c) shows scanning electron microscopy (SEM) images of the nanopatterned ITO electrode (top) and the deposited organic layer stack (bottom) in type A devices, while d) shows AFM images of the nanopatterned imprint resist (top) and the fluorescent waveguide (bottom). In both device types, the periodicity of the one-dimensional nanograting structure is preserved throughout the layer sequence.

combination with a conventional OLED. In this device structure, the fluorescent layer acts as a color conversion layer (CCL) reemitting light into the waveguide. Spatial separation from the typically lossy electrode materials ensures a high-quality factor leading to narrow-angle emission of the fluorescent light.

In this work, we compare light emission characteristics from two types of directional OLEDs, namely OLEDs comprising a periodic nanopattern etched into the ITO electrode (OLED type A) and conventional OLEDs featuring a periodically nanopatterned fluorescent waveguide layer deposited on the substrate backside (OLED type B), by simulation and experimental methods. Figure 1 shows the two device structures under investigation including scanning electron microscopy (SEM) and atomic force microscopy (AFM) images of the fabricated samples.

2. Device Design and Fabrication

We used the same fluorescent polymers as the emissive layer in OLEDs of type A and as the fluorescent waveguide layer in OLEDs of type B so as to be able to directly compare the emission characteristics of the different OLED types. Specific combinations of emission wavelength and angle can be obtained by the appropriate choice of polymer emission spectrum and nanopattern design. The polymers chosen in this study are Poly(9,9-dioctylfluorene-alt-benzothiadiazole) (F8BT) and Poly[2-methoxy-5-(2′-ethylhexyloxy)-1,4-phenylene vinylene] (MEH-PPV). The complex refractive indices of the polymer thin films as well as their photoluminescence (PL) emission spectra are shown in **Figure 2**.

The two polymer compounds were chosen expecting a considerable difference between green (F8BT) and orange/red (MEH-PPV) emission.[20] The F8BT material batch used for this study, however, exhibited orange light emission, resulting in similar emission spectra for both compounds. While a blend of F8BT and PFO (Poly(9,9-di-n-octylfluorenyl-2,7-diyl)), which is commonly used for polymer OLEDs,[21] yielded the expected green emission color, the absorption spectrum of PFO was not suitable for type B devices. Electroluminescence (EL) spectra of the OLED devices may additionally show slight deviations from the PL spectra of the isolated polymer layers due to the optical cavity formed by the electrode layers.

Resonant light coupling in photonic crystal structures is a well-understood phenomenon. The intensity and shape of the resonance effects depend on the optical properties of the waveguide itself as well as the periodic nanopattern.[22] In type A OLEDs, the waveguide is formed by the ITO bottom electrode plus the organic layer stack and is bounded by the metallic top electrode. In type B OLEDs, the waveguide only comprises the fluorescent polymer layer. Isolated comparison of different waveguide configurations is only possible if the geometric parameters of the integrated nanopatterns are effectively identical. To achieve high structural conformity, we employed the UV nanoimprint lithography process detailed in ref. [23] utilizing a single master stamp holding a 1D grating with a period length of 370 nm and a grating depth of 60 nm for nanopattern generation on all samples. For the imprinting steps, secondary PDMS (polydimethylsiloxane) stamps were fabricated, which featured a slightly reduced period length of 362 nm due to
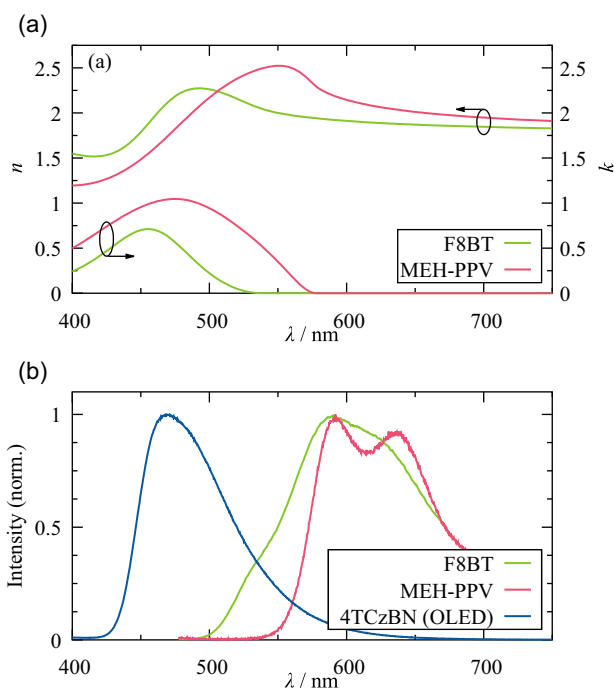

Figure 2. a) Refractive indices measured by white-light ellipsometry. b) Emission spectra of F8BT and MEH-PPV compared to the emission spectrum of the excitation OLED. Efficient excitation of the fluorescent films is expected because of good agreement between the extinction coefficient k and the emission peak of the blue OLED.

the thermal shrinkage of the silicone. The resulting, virtually identical, nanogratings were subsequently used as templates for patterning of the waveguide materials. The exact agreement of the final nanopatterns in both device types, however, was not obtainable as the respective nanopattern placement required different fabrication approaches.

Nanopatterned ITO layers for OLEDs of type A were fabricated by ion beam etching using the patterned nanoimprint resist as an etching template. Process details and parameters were the same as described in ref. [24] The grating depth of the nanopattern in the electrode layer is reduced to 50 nm owing to differences in the etching rates of the imprint resist and ITO. The grating period and the general pattern shape, on the other hand, are preserved throughout the etching process. The organic layer stack consisting of poly(3,4-ethylenedioxythiophene) polystyrene sulfonate (PEDOT:PSS, 50 nm) and either F8BT or MEH-PPV (70 nm) was subsequently deposited onto the nanopatterned ITO electrode by spin-coating. Finally, a 1 nm thick layer of LiF and a 150 nm Al cathode were thermally evaporated.

While OLEDs with nanopatterned CCLs aiming at white light emission have already been reported, they typically show low directionality due to the residual OLED emission.[25] To utilize most of the excitation light and suppress nondirectional blue background emission in type B OLEDs, we employed highly absorbent fluorescent layers with a thickness between 200 and 300 nm, which is significantly higher than in the organic stack of type A devices. We used a blue OLED comprising the emissive material 2,3,5,6-Tetrakis(3,6-di-*tert*-butyl-9 H-carbazol-9-yl)benzonitrile (4TCzBN)

as the excitation source, matching the absorption spectra of F8BT and MEH-PPV.

Blue excitation OLEDs for devices of type B were fabricated by thermal evaporation on glass substrates employing the following device stack: ITO (140 nm) | 1,4,5,8,9, 11-Hexaazatriphenylenehexacarbonitrile (HATCN, 5 nm) | 1,1-Bis[(di-4-tolylamino)phenyl]cyclohexane (TAPC, 35 nm) | 1,3-Bis(N-carbazolyl)benzene (mCP) doped with 4TCzBN (20%, 25 nm) | Diphenyl[4-(triphenylsilyl)phenyl]phosphine oxide (TSPO1, 5 nm) | 2,2′,2″-(1,3,5-Benzinetriyl)-tris (1-phenyl-1-H-benzimidazole) (TPBi, 30 nm) | LiF (1 nm) | Al (150 nm). OLED fabrication was followed by the formation of the nanopatterned CCL. For this purpose, a nanograting template was deposited on the backside of the OLED substrate by UV nanoimprint lithography, as mentioned earlier. This bottom layer was subsequently covered by spin-coating either F8BT or MEH-PPV from their respective solutions in toluene, forming a nanopatterned waveguide.

The nanogratings integrated into the different waveguide configurations are identical except for a 10 nm difference in grating height. We believe this deviation to be negligible because the grating height is expected to mainly affect the spectral width of the resonance effect. Further discrepancy between the photonic crystal slabs may arise due to the deposition of the waveguide material. In both type A and type B devices, polymer layers are spin-coated onto the nanograting, leading to the filling of the nanopattern.[26] As confirmed by the AFM measurement shown in Figure 1, the top side of the polymer layer exhibits an attenuated grating structure with reduced grating height and rounded feature shapes. The grating attenuation effect is anticipated to be less pronounced in type A devices, since the organic layer stack thickness is considerably lower than the waveguide thickness in type B devices.

3. Simulation Results

We simulated the radiation patterns of both OLED types using the finite-difference time-domain method (Ansys Lumerical FDTD) in combination with a reciprocity-based far-field calculation method.[27,28] Following this approach, the structure is excited by plane waves that represent the incident field of distant dipoles in the far field. The resulting fields are measured in the emissive layer. By means of the reciprocity principle, the results of the reciprocal situation, i.e., dipole emitters in the active area and field monitors in the far field, can be calculated. We employed Lumerical's BFAST plane wave source for accurate broadband plane wave injection at all injection angles.[29] Because the nanopatterns are 1D, it is sufficient to simulate 2D unit cells of the periodically patterned devices. The simulated structures are depicted in **Figure 3**.

In all cases, the simulation region is bounded by perfect electric conductors (PEC) at the top and bottom and BFAST boundary conditions at the left and right boundary. Perfectly matched layers (PMLs) are used to emulate reflexionless radiation into the far field. We used the measured refractive indices shown in Figure 3 for MEH-PPV and F8BT and data from the literature for the remaining OLED materials.[30–35] To stabilize the simulation in cases of ultra high-Q resonances in the transparent
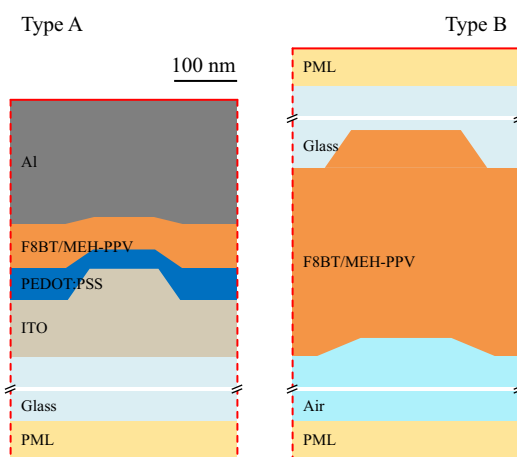

Figure 3. Simulated device structures of type A and B OLEDs. The grating attenuation shown in Figure 1 is taken into account in the model. The air and glass layer thicknesses are not to scale. Their thickness in the simulation is 1 μm to keep the perfectly matched layers (PMLs) at a distance from the near fields around the nanostructures. The plane wave sources necessary for the reciprocity-based simulation are placed a few mesh cells above the bottom PML. 2D field monitors are placed on the F8BT/MEH-PPV layers.

windows ($\lambda > 600$ nm for MEH-PPV and $\lambda > 550$ nm for F8BT), where $k = 0$, we added a small absorption $k = 0.003$ to the measured complex refractive indices. Note that real devices will always suffer from additional losses due to incoherent scattering at geometric irregularities, which are otherwise not included in the simulation. For type A structures, the entire OLED stack containing the emissive polymer layer is considered in the simulation. For type B structures, the fluorescent layer is assumed to be excited homogeneously by the blue OLED. Therefore, the excitation is not included in the simulation of type B devices. Instead, we simulated only the emission from dipoles in the nanopatterned fluorescent waveguide.

TM modes are expected to be barely excited because the dominant emitter dipole orientation in spin-coated conjugated polymer layers is in plane.[36] Therefore, we simulated only the radiation patterns from emitter dipoles oriented parallel to the grating lines, which excite only TE modes. In the simulations, it is assumed that emitting dipoles are homogeneously distributed in the emission layer. To get quantitatively comparable results, the far fields are normalized by the emission layer area.

The simulation results are shown in **Figure 4**.

Strong resonant outcoupling peaks can be seen for both type B OLEDs with the nanopatterned fluorescence layer, while type A OLEDs exhibit only weak outcoupling resonances. The resonance quality factor depends mainly on the refractive index contrast introduced by the nanograting and the optical mode's propagation length inside the waveguide. Since the respective emissive materials are the same in type A and B OLEDs, resonance intensity is directly comparable. The distinct differences between the two device designs can therefore be explained as follows: The additional OLED layers in type A devices (ITO, PEDOT:PSS, and Al) cause increased absorption of the quasiguided modes, lowering their propagation length. Additionally,
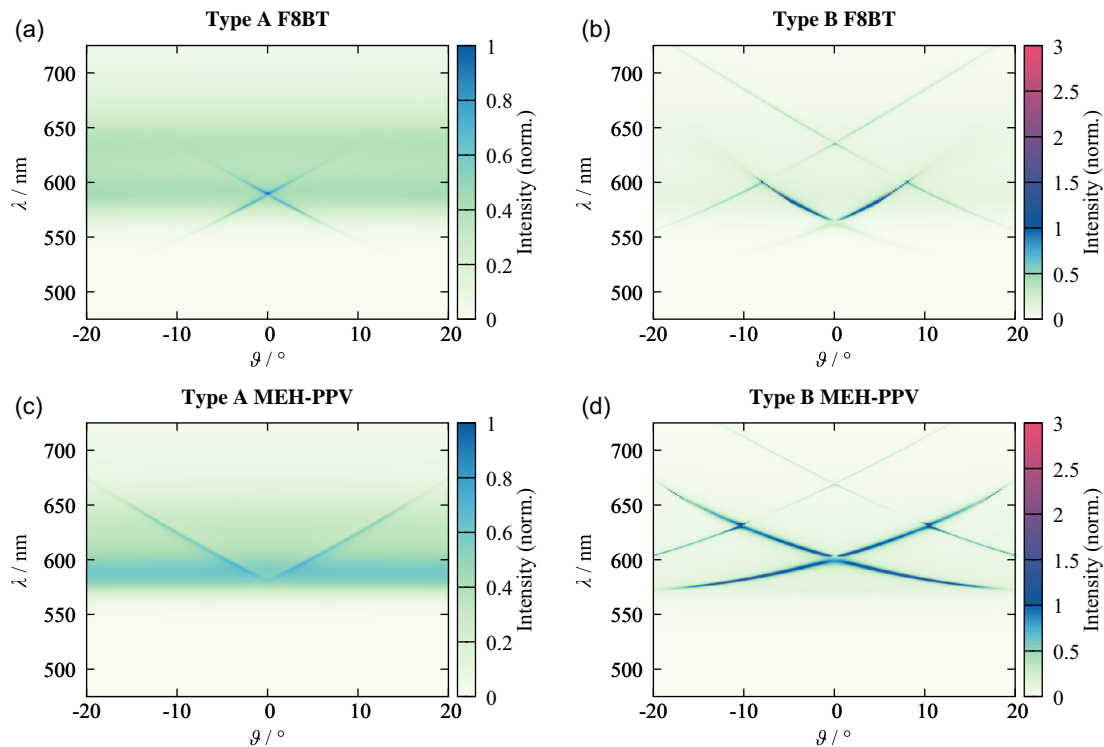
Figure 4. Simulated angle-resolved emission characteristics of type A and type B devices with a,b) F8BT and c,d) MEH-PPV emissive layers. Emission intensities are normalized globally, thus the results are quantitatively comparable. Colorbar settings have been adjusted for better perceptibility, because resonant outcoupling effects are significantly stronger in type B devices (right side).

the initially nanopatterned interface in type A devices is located between the ITO electrode and the organic layer stack containing the high-index polymer, resulting in a comparatively low refractive index modulation. The fluorescent waveguide in type B OLEDs, in contrast, is deposited on the nanoimprint resist ($n \approx 1.51$) leading to a significantly higher optical contrast. Consequently, the resonance strength is expected to be much higher in the type B structure. Furthermore, both type B devices show two TE resonances (TE_0 and TE_1) due to the higher layer thickness. The TE_0 mode's field is strongly confined in the center of the high index layer, leading to weak interaction with the grating. As a result, the TE_0 modes show extremely high-quality factors ($Q \approx 400$ for the F8BT waveguide and $Q \approx 2000$ for the MEH-PPV waveguide), which may render them invisible in the experiment.

4. Experimental Results

We recorded angle-resolved emission spectra of the fabricated OLED devices in 1° steps using an in-house built goniophotometer setup. TE and TM resonance peaks were differentiated experimentally by placing a linear polarization filter in front of the detector. Comparison with the simulated resonance positions yielded the corresponding quasi-guided mode order. To allow for direct compatibility of the resonance effects irrespective of OLED efficiency and brightness, we excited the emissive photonic crystal structures optically with an external light source matching the polymers'

absorption spectra. For this, the entire device area was homogeneously illuminated by a blue LED with an emission maximum around 455 nm (M455D3, Thorlabs), which was fixed on the rotational stage of the goniophotometer setup to obtain identical excitation strength for all viewing angles. The resulting PL emission spectra for the two device types employing F8BT and MEH-PPV as the emissive material, respectively, are depicted in **Figure 5**.

For comparison, emission spectra of the OLEDs in electrical operation were also measured using the same goniophotometer setup and an external source measure unit to operate the OLEDs at a constant current density (see **Figure 6**).

The contrast in resonance quality between the OLED types observable in the experiment is even more pronounced than suggested by the simulation. Differences in resonance positions between the simulation and experiment can be attributed to deviations in the refractive indices and the fact that the simulation used isotropic material parameters for simplicity. Devices of type A exhibit barely recognizable resonance effects which are strongly dominated by nondirectional fluorescence emission at all viewing angles. In contrast, the PL emission spectra of devices of type B feature sharp outcoupling peaks owing to the significantly higher resonance quality factor, as described above. Moreover, the resonance position in type B devices is located at higher wavelengths (compared to type A devices) due to the increased waveguide layer thickness and the larger amount of the high-index polymer.

Similar to the simulation, a single resonant TE mode is observable for the type A devices, while the type B F8BT sample
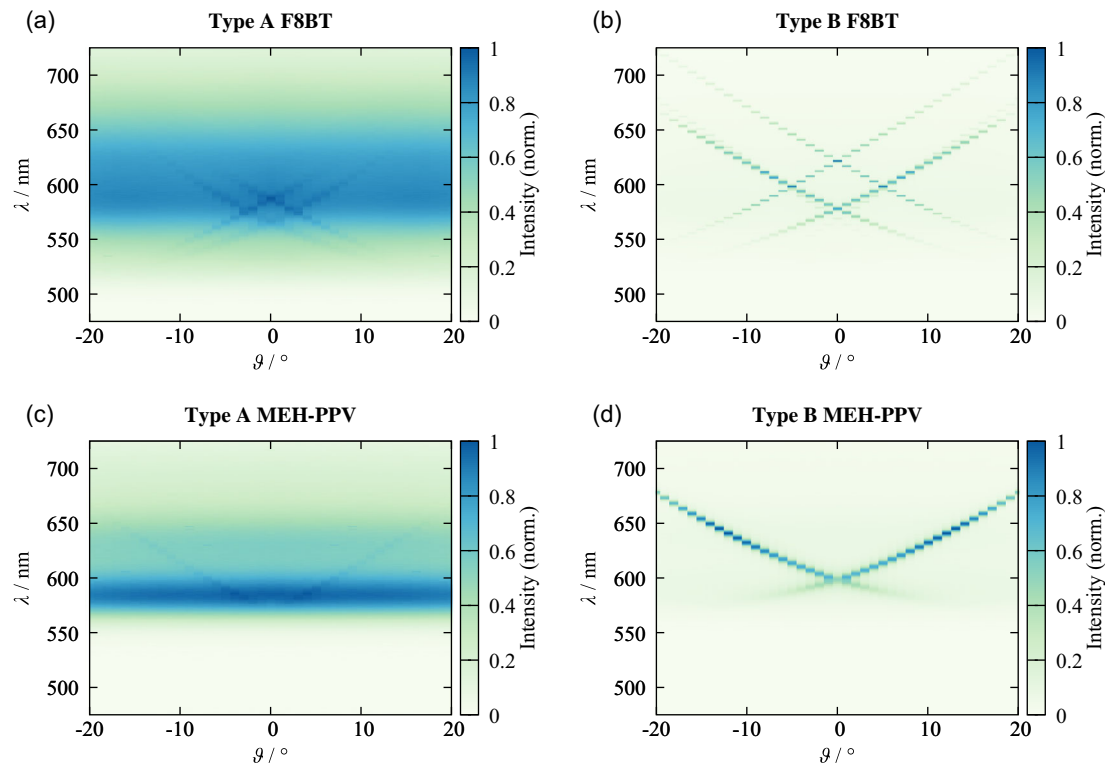
**ADVANCED
SCIENCE NEWS**
www.advancedsciencenews.com

**ADVANCED
PHOTONICS
RESEARCH**
Open Access
www.adpr-journal.com

Figure 5. Angle-resolved PL emission spectra of the OLED devices under investigation with a,b) F8BT and c,d) MEH-PPV emissive layers. Type A devices (left side) show minimal resonant outcoupling effects while type B devices (right side) exhibit high resonance quality. Similar to the simulation results shown in Figure 4, nondirectional background emission is almost exclusively visible in type A devices.

(b) features two TE modes ($Q \approx 370$ for the TE_0 mode and $Q \approx 210$ for the TE_1 mode). However, the TE_0 mode in the type B MEH-PPV sample (d), which is located around $\lambda \approx 670$ nm at $\vartheta = 0°$ according to the simulation and expected to have a quality factor in the range of $Q \approx 2000$, is not visible in the experiment. We attribute this deviation to the extremely high-quality factor of the MEH-PPV waveguide's TE_0 mode. This high Q factor corresponds to a very weak coupling to the far field (and very low absorption), which requires a long propagation length to form a notable outcoupling peak. Incoherent scattering effects due to structural irregularities (creating broadband, omnidirectional emission) limit the mode propagation and therefore the formation of a defined outcoupling peak.

Both waveguides containing F8BT allow for the formation of a relatively weak TM mode, which is clearly visible in the 0° emission spectra shown in Figure 6 ($\lambda \approx 570$ nm in the type A device and $\lambda \approx 580$ nm in the type B device). Due to the refractive index anisotropy of the polymer layer, the order of the effective refractive indices of TE and TM modes can differ from the alternating pattern found in isotropic slab waveguides. TM modes are not accounted for in the simulation, as only emitter dipoles coupling into TE modes are considered.

EL and PL emission characteristics of the polymer layers in devices of type A are similar because the general device structure remains unchanged. Slight differences may arise as the location of the emission zone inside the thin film during electrical operation is determined by charge recombination.

Nevertheless, significant enhancement of resonant outcoupling cannot be expected.[37] The intensity of the outcoupling effects can most easily be assessed by comparing emission spectra at a fixed outcoupling angle (corresponding to a vertical cut in the angle-resolved emission spectra), as shown in Figure 6. In accordance with the angle-resolved emission characteristics, a small TE resonance peak at $\lambda = 580$ nm is observable for the type A F8BT device exhibiting a slightly sharper profile in the electroluminescence measurement. For the type A MEH-PPV device no resonance effects are visible at $\vartheta = 0°$.

Fluorescence emission and resonance intensity of type B devices are expected to be identical for PL and EL measurements as the nanopatterned CCL is optically excited in both cases. Differences in the emission spectra are due to residual OLED emission, which reduces overall emission directionality. In comparison, the F8BT waveguide layer exhibits a higher quality factor than the MEH-PPV waveguide, apparent by the significantly sharper resonance peaks. Additionally, suppression of nondirectional OLED background light is higher, resulting in light outcoupling at extremely narrow cone angles for specific wavelengths. Although the MEH-PPV CCL features a higher transmission of the OLED excitation light, emission directionality is still high. While the broader shape of the resonance peak results in slightly lower wavelength selectivity, the increase in spectral bandwidth of the resonance enhances the total amount of light coupled into a specific direction.
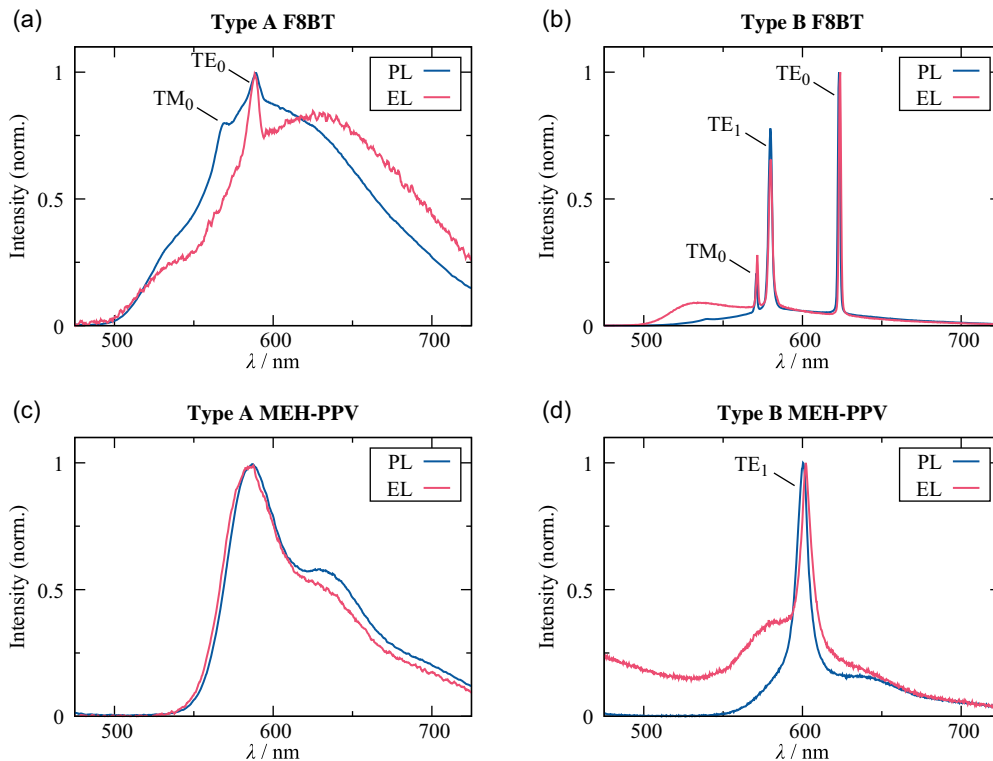
**ADVANCED
SCIENCE NEWS**

www.advancedsciencenews.com

**ADVANCED
PHOTONICS
RESEARCH**
Open Access

www.adpr-journal.com

Figure 6. Comparison between emission spectra of the investigated OLED devices with a,b) F8BT and c,d) MEH-PPV emissive layers at $\vartheta = 0°$ under optical and electrical operation. Differences between PL and EL spectra may arise due to confinement of the emission zone (type A devices) or residual transmission of the OLED excitation light (type B devices). The TM_0 mode seen in the Type B F8BT device is not located between the TE_0 and TE_1 mode due to the material's anisotropy.

Directional light outcoupling from our type A devices is significantly lower than reported for similar devices employing different organic layer stacks.[15,38] Consequently, we fabricated entirely thermally evaporated OLEDs on top of the nanopatterned ITO electrodes to reevaluate the suitability of our fabrication approach. The corresponding angle-dependant emission characteristics presented in **Figure 7** show clearly recognizable resonant outcoupling effects and directional light emission. We, therefore,
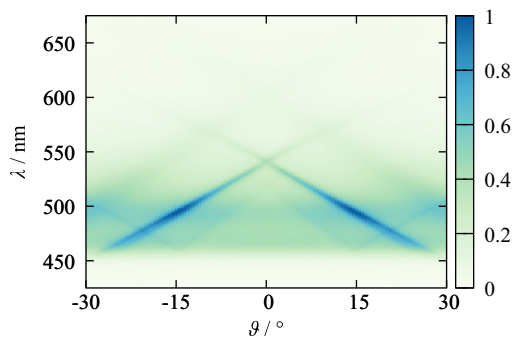

Figure 7. Angle-resolved EL spectrum of a type A OLED fabricated by thermal evaporation comprising a nanopatterned ITO electrode. Resonant outcoupling effects are strongly visible, indicating that the quality of the etched ITO photonic crystal structure is sufficient for highly directional light outcoupling.

attribute the low resonance quality of the photonic crystal structures in the solution-processed OLEDs to the organic layer stack itself. As mentioned previously, the dominant refractive index modulation in this device structure usually occurs at the interface between the ITO bottom electrode ($n \approx 2$) and the organic semiconducting layers (typically $n \approx 1.61.8$). Since the polymer materials used in this work also exhibit high refractive indices close to 2, the optical contrast is reduced, leading to lower resonance intensity. Type B devices, in contrast, feature a separate nanopatterned high-index waveguide layer providing strong refractive index modulation at the interface between the fluorescent polymer and the imprint resist.

Polar plots of the integrated emission intensity for both types of devices are depicted in **Figure 8**.

Type A devices exhibit wide-angle emission characteristics similar to the ideal Lambertian emission pattern. In contrast, type B devices show distinct deviations from the Lambertian emission shape. Increased light outcoupling is observable at viewing angles up to 30°, which is in accordance with the resonance effects visible in Figure 5. In the investigated samples, light outcoupling is enhanced mainly in the forward direction, i.e., perpendicular to the substrate surface. Directional emission into higher viewing angles is obtainable by altering the period length of the nanopattern to shift the resonance position.

In many application scenarios, additional spectral filtering is introduced due to different system components such as
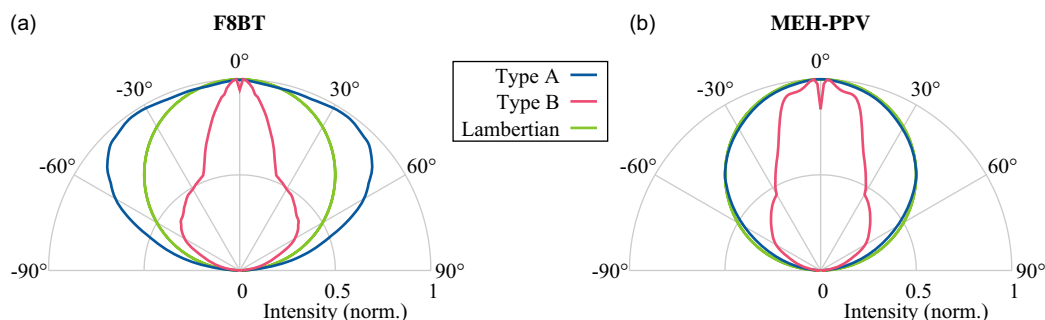
Figure 8. Integrated polar plots of the emission characteristics of OLEDs with a) F8BT and b) MEH-PPV emissive layers in photoluminescence. Type B devices feature directional forward emission with a distinct intensity dip at $\vartheta = 0°$ which can be attributed to the optical bandgap of the photonic crystal slab.
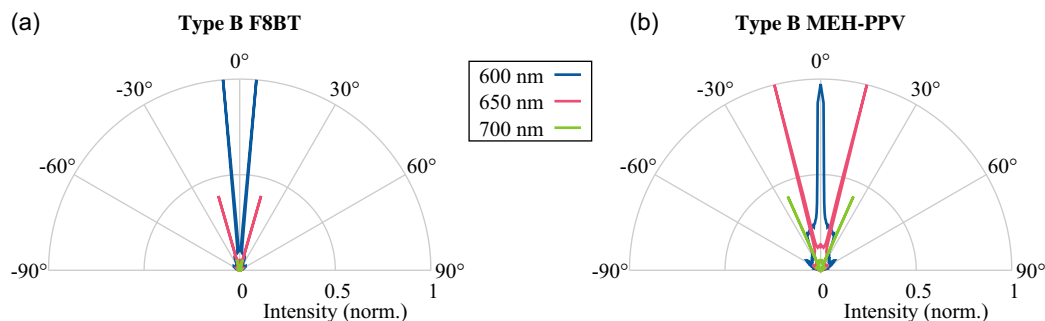

Figure 9. Polar plots of the EL emission characteristics of type B OLED devices with a) F8BT and b) MEH-PPV CCLs at specific wavelengths. Highly directional emission into extremely narrow cone angles is obtained for both fluorescent materials.

narrow-band absorption of analyte compounds or wavelength-dependent photodetector sensitivity. In either case, only a limited wavelength range of the emission spectrum is effectively utilized. Assuming spectral restrictions of the overall sensing system, highly directional light emission into narrow cone angles can be obtained. Polar plots of the emission intensity at specific wavelengths highlighting this effect are shown in **Figure 9**.

5. Conclusions

In this work, we compare two different approaches to obtain directional emission from OLED devices employing photonic crystal slabs. In type A devices, the periodic nanopattern is directly integrated into the OLED stack by patterning the ITO bottom electrode before device fabrication. In type B, devices a conventional OLED is combined with a nanopatterned color conversion layer deposited on the substrate backside. Despite using the same fluorescent polymers (F8BT and MEH-PPV) as the emissive layer in both approaches, differences in resonant outcoupling intensity arise due to the different waveguide properties. Optical absorption in the additional OLED layers limits the resonance quality factor of the photonic crystal slab in type A devices. Additionally, the refractive index contrast between the nanopatterned electrode and the high-index polymer layers is low, resulting in negligible directional light outcoupling. In type B devices, on the other hand, sharp outcoupling peaks are observable at specific wavelengths and viewing angles. Integrated emission spectra show forward directionality, whereas directional

emission into higher viewing angles is obtainable by spectral filtering.

Conflict of Interest

The authors declare no conflict of interest.

Author Contributions

J.B.: Experiment conceptualization and design, sample fabrication and characterization, visualization, original draft preparation, review, and editing; H.L.: Simulation design and implementation, ellipsometry data fitting, manuscript preparation (simulation section), review, and editing; G.B.: Sample fabrication and characterization (Figure 7 OLED); T.N.: Parameter studies; A.P.: AFM measurements; M.G.: Concept, funding acquisition, project administration and supervision, review, and editing.

Data Availability Statement

The data that support the findings of this study are available from the corresponding author upon reasonable request.

[1] G. Gong, Z. Shen, P. E. Burrows, S. R. Forrest, *Adv. Mater.* **1997**, *9*, 725.

[2] H. W. Chen, J. H. Lee, B. Y. Lin, S. Chen, S. T. Wu, *Light: Sci. Appl.* **2017**, *7*, 17168.

[3] S. Reineke, F. Lindner, G. Schwartz, N. Seidler, K. Walzer, B. Lüssem, K. Leo, *Nature* **2009**, *459*, 234.

[4] M. Eritt, C. May, K. Leo, M. Toerker, C. Radehaus, *Thin Solid Films* **2010**, *518*, 3042.

[5] R. Liu, Y. Cai, J.-M. Park, K.-M. Ho, J. Shinar, R. Shinar, *Adv. Funct. Mater.* **2011**, *21*, 4744.

[6] I. Titov, M. Kopke, N. C. Schneidewind, J. Buhl, Y. Murat, M. Gerken, *IEEE Sens. J.* **2020**, *20*, 7540.

[7] I. Titov, M. Köpke, M. Gerken, *Sensors* **2022**, *22*, 910.

[8] J. Buhl, H. Lüder, T. Nolte, F. O. Sbrisny, M. Gerken, in *Organic Photonic Materials And Devices XXIV*, Vol 11998, (Eds: W. M. Shensky III, I. Rau, O. Sugihara), International Society for Optics and Photonics, SPIE, Bellingham, WA **2022** pp. 1–8.

[9] S. H. Kim, S. K. Kim, Y. H. Lee, *Phys. Rev. B* **2006**, *73*, 235117.

[10] C. Wiesmann, K. Bergenek, N. Linder, U. T. Schwarz, *Laser Photon. Rev.* **2009**, *3*, 262.

[11] G. A. Turnbull, P. Andrew, M. J. Jory, W. L. Barnes, I. D. W. Samuel, *Phys. Rev. B* **2001**, *64* 125122.

[12] J. M. Lupton, B. J. Matterson, I. D. Samuel, M. J. Jory, W. L. Barnes, *Appl. Phys. Lett.* **2000**, *77*, 3340.

[13] K. Ishihara, M. Fujita, I. Matsubara, T. Asano, S. Noda, H. Ohata, A. Hirasawa, H. Nakada, N. Shimoji, *Appl. Phys. Lett.* **2007**, *90*, 111114.

[14] J. Hauss, T. Bocksrocker, B. Riedel, U. Lemmer, M. Gerken, *Opt. Express* **2011**, *19*, A851.

[15] U. Geyer, J. Hauss, B. Riedel, S. Gleiss, U. Lemmer, M. Gerken, *J. Appl. Phys.* **2008**, *104*, 93111.

[16] T. Schwab, C. Fuchs, R. Scholz, A. Zakhidov, K. Leo, M. C. Gather, S. Reineke, F. Lindner, G. Schwartz, N. Seidler, K. Walzer, B. Lüssem, K. Leo, Z. B. Wang, M. G. Helander, J. Qiu, D. P. Puzzo, M. T. Greiner, Z. M. Hudson, S. Wang, Z. W. Liu, Z. H. Lu, *Opt. Express* **2014**, *22*, 7524.

[17] Y. S. Shim, J. H. Hwang, C. H. Park, S. G. Jung, Y. W. Park, B. K. Ju, *Nanoscale* **2016**, *8*, 4113.

[18] A. Lasagni, B. Lüssem, C. Fuchs, K. Leo, L. Müller-Meskamp, M. C. Gather, R. Scholz, S. Eckardt, S. Hofmann, T. Roch, T. Schwab, *Opt. Express* **2013**, *21*, 16319.

[19] S. Zhang, G. A. Turnbull, I. D. W Samuel, *Adv. Opt. Mater.* **2014**, *2*, 343.

[20] Z. Hashim, S. Alomari, W. Alghamdi, R. Altuwirqi, M. Green, *RSC Adv.* **2017**, *7*, 48308.

[21] J. Morgado, R. H. Friend, F. Cacialli, *Appl. Phys. Lett.* **2002**, *80*, 2436.

[22] S. Fan, J. D. Joannopoulos, *Phys. Rev. B* **2002**, *65*, 235112.

[23] S. Jahns, M. Bräu, B.-O. Meyer, T. Karrock, S. B. Gutekunst, L. Blohm, C. Selhuber-Unkel, R. Buhmann, Y. Nazirizadeh, M. Gerken, *Biomed. Opt. Express* **2015**, *6*, 3724.

[24] J. Buhl, D. Yoo, M. Köpke, M. Gerken, *Nanomanufacturing* **2021**, *1*, 39.

[25] Y.-H. Ho, D.-W. Huang, Y.-T. Chang, Y.-H. Ye, C.-W. Chu, W.-C. Tian, C.-T. Chen, P.-K. Wei, *Opt. Express* **2012**, *20*, 3005.

[26] B. Riedel, J. Hauss, U. Geyer, J. Guetlein, U. Lemmer, M. Gerken, *Appl. Phys. Lett.* **2010**, *96*, 243302.

[27] O. T. A. Janssen, A. J. H. Wachters, H. P. Urbach, *Opt. Express* **2010**, *18*, 24522.

[28] S. Zhang, E. R. Martins, A. G. Diyaf, J. I. B. Wilson, G. A. Turnbull, I. D. W. Samuel, *Synth. Metals* **2015**, *205* 127.

[29] B. Liang, M. Bai, H. Ma, N. Ou, J. Miao, *IEEE Trans. Antennas Propag.* **2014**, *62*, 354.

[30] T. A. F. König, P. A. Ledin, J. Kerszulis, M. A. Mahmoud, M. A. El-Sayed, J. R. Reynolds, V. V. Tsukruk, *ACS Nano* **2014**, *8*, 6182.

[31] Refractive Index of In_2O_3-SnO_2 (Indium tin oxide, ITO) – Konig, https://refractiveindex.info/?shelf=other&book=In2O3-SnO2&page=Konig (accessed: December 2021).

[32] C.-W. Chen, S.-Y. Hsiao, C.-Y. Chen, H.-W. Kang, Z.-Y. Huang, H.-W. Lin, *J. Mater. Chem. A* **2015**, *3*, 9152.

[33] Refractive index of PEDOT:PSS - Chen, https://refractiveindex.info/?shelf=other&book=PEDOT-PSS&page=Chen (Accessed: March 2022).

[34] K. M. McPeak, S. V. Jayanti, S. J. P. Kress, S. Meyer, S. Iotti, A. Rossinelli, D. J. Norris, *ACS Photonics* **2015**, *2*, 326.

[35] Refractive index of Al (Aluminium) - McPeak, https://refractiveindex.info/?shelf=main&book=Al&page=McPeak (Accessed: March 2022).

[36] H. Becker, S. E. Burns, R. H. Friend, *Physical Review B* **1997**, *56*, 1893.

[37] H. Lüder, J. Buhl, M. Gerken, in *Physics And Simulation Of Optoelectronic Devices XXX*, Vol 11995 (Eds: B. Witzigmann, M. Osiński, Y. Arakawa), International Society for Optics and Photonics, SPIE, Bellingham, WA **2022**, pp. 69–77.

[38] M. Fujita, K. Ishihara, T. Ueno, T. Asano, S. Noda, H. Ohata, T. Tsuji, H. Nakada, N. Shimoji, *Jpn. J. Appl. Phys.* **2005**, *44*, A3669.